

SUPPORTING INFORMATION

Edge Effect of Strained Bilayer Nanofilms for Tunable Multistability and Actuation

Nan Hu¹, Xiaomin Han¹, Shicheng Huang¹, Hannah Grover¹, Xiaojiao Yu¹, Lina Zhang^{1,2}, Ian Trase¹, John X.J. Zhang¹, Li Zhang^{3}, Lixin Dong^{4*}, Zi Chen^{1*}*

¹ Thayer School of Engineering, Dartmouth College, Hanover, NH 03755, United States

² Department of Engineering Mechanics, Shanghai Jiao Tong University, Shanghai 200240, China

³ Department of Mechanical and Automation Engineering, Chinese University of Hong Kong, Shatin, N.T. 999077, Hong Kong SAR, China

⁴ Department of Electrical and Computer Engineering, Michigan State University, East Lansing, MI 48823, United States

*To whom correspondence should be addressed

1. Nanofabrication and Nanorobotic Manipulation

The micro-claw (with "X" shape) is patterned from Si/Cr bilayers, grown on Si (001) substrate. Each "finger" orients along either the [100] or [010] direction and is an isosceles triangle, with a 4 μm long base and two 8 μm long edges. The angle between an edge and the base is 75.5°. The total thickness of the micro-claw is 45 nm. A 35 nm thick p-type Si layer was epitaxially grown by ultrahigh vacuum chemical vapor deposition (UHV-CVD) on Si (001) at 550 °C followed by the deposition of a 10-nm thick amorphous Cr layer by e-gun evaporation. E-beam lithography, reactive ion etching (RIE), and wet etching were applied to form the rolled-up silicon–metal (Si/Cr) hybrid structures on Si (001). The Si/Cr nanostructures were imaged with a field emission scanning electron microscope (FESEM) Zeiss SUPRA 55VP. A nanorobotic manipulator (MM3A™ from Kleindiek) installed inside a scanning electron microscope (SEM) (Zeiss DSM962) was used for the manipulation experiments. ¹

2. Table-top Experiment

A piece of a layered stainless steel measuring tape (11 mm long, 25.4 mm wide and 0.127 mm thick) was tapered on both ends to resemble two opposite micro-claw fingers, with the same edge-to-base angle, as shown in Figure S1a. A uniaxial stress perpendicular to the long axis of the tape has induced intrinsic curvature oriented along the long axis. If we curl the object around an axis perpendicular to the long axis (starting at the tip of the tape) and then remove the stimulus, it will snap back to its initial configuration, indicating monostability. In order to create bistability, we introduce a curvature perpendicular to the long axis with opposite sign by folding the triangular sections of the tape around a dowel. The triangular part then has a stress state similar to the micro-claw finger. The middle section of the specimen only has a uniaxial stress in the lateral direction, so while the triangular parts have two stable states the middle part only has one.

Figure S1b shows that when we touched one finger it changed from the open to closed state, indicating bistability. Similar to the nanorobotic manipulation, another finger can be triggered in the same way such that both fingers are in the closed state (see Figure S1c and S1d). The bistability is dependent on the applied uniaxial stress along the long axis, which is a function of dowel diameter. If this stress is too small, the specimen cannot overcome the energy barrier and remains monostable in the open state. If this stress is too large, the measuring tape will be monostable in the closed state.

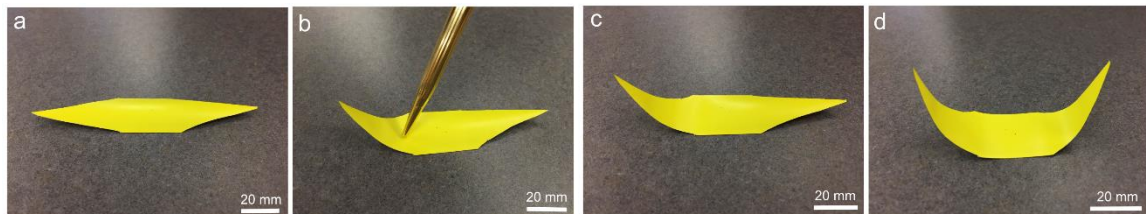


Figure S1. Table-top experiments on the snap-through of a bistable tape. (a). an open stable state; (b) mechanical stimulus; (c) the left finger in the closed state, the right finger in the open state; (d) both fingers in the closed state.

3. Theoretical analysis

The expression for the total energy in the thin plate is

$$\Pi = \iint^{z=H/2} (f_1 \gamma_{xx} + f_2 \gamma_{yy}) dt dy + \iint^{z=-H/2} f_1^e \gamma_{xx} dt dy + \frac{1}{2} \int_{-H/2}^{H/2} dz \iint \left[\frac{E}{1+\nu} (\gamma_{xx}^2 + \gamma_{yy}^2 + \gamma_{zz}^2) + \frac{E\nu}{(1+\nu)(1-2\nu)} (\gamma_{xx} + \gamma_{yy} + \gamma_{zz})^2 \right] dt dy$$

In the expression, the term $\iint^{z=H/2} (f_1 \gamma_{xx} + f_2 \gamma_{yy}) dt dy$ is the surface energy for the top surface.

The integral $\iint dt dy$ is the shape of a triangle.

$$\iint dt dy = \int_{g+2g\frac{w_0}{w}}^0 dy \int_{-y(w+2w_0)/2/(g+2g\frac{w_0}{w})}^{y(w+2w_0)/2/(g+2g\frac{w_0}{w})} dt$$

The term $\int_e (f_1^e \gamma_{xx}) dt dy$ is the surface energy for the middle regime on the bottom surface. As shown in the Figure S2, the width of the bottom layer is slightly shorter than the top layer due to the under-stretching.

The integral of bottom surface energy is $\oint_e dt dy = 2 \int_g^0 dy \int_{-yw/2g}^{yw/2g} dt$

The term $\frac{1}{2} \int_{-H/2}^{H/2} dz \iint \left[\frac{E}{1+\nu} (\gamma_{xx}^2 + \gamma_{yy}^2 + \gamma_{zz}^2) + \frac{E\nu}{(1+\nu)(1-2\nu)} (\gamma_{xx} + \gamma_{yy} + \gamma_{zz})^2 \right] dt dy$ is the strain energy, which later can be divided into stretching and bending energy.

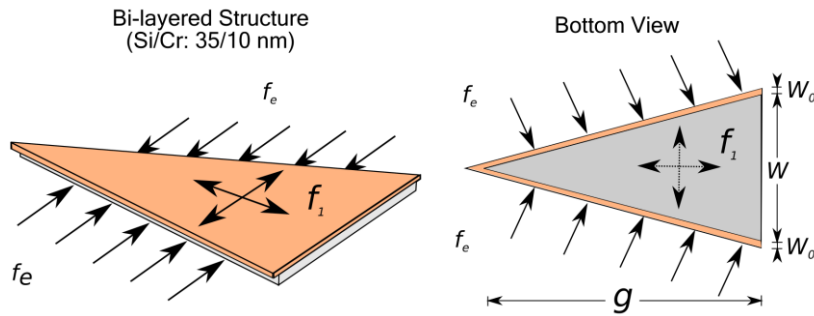


Figure S2. Schematic diagram for the finger of the micro-claw.

f_e is the surface stress on the bottom surface. It is along y-direction. The width of the edge in the horizontal direction is w_0 , the total horizontal length is $w + 2w_0$. The height for the middle regime is g . The total height is $g + 2g \frac{w_0}{w}$

The strain components are the following²

$$\gamma_{xx}(t, z) = \frac{[\cos(\kappa_2 t) z]}{\left\{ \frac{1}{\kappa_1} + \frac{[\cos(\kappa_2 t) - 1]}{\kappa_2} \right\}} + [\cos(\kappa_2 t) - 1] \kappa_1 / \kappa_2$$

$$\gamma_{yy}(t, z) = \kappa_2 z$$

$$\gamma_{zz}(t, z) = -\frac{\nu}{1 - \nu} (\gamma_{xx} + \gamma_{yy})$$

We plug in the expressions of strain into the energy expression and integrate to obtain the stretching energy and the bending energy:

$$\Pi_g = \frac{Egh(\kappa_1 \kappa_2)^2 (w + 2w_0)^6}{3840w(1 - \nu^2)}$$

$$\Pi_b = \frac{Egh^3 (w + 2w_0)^2 (\kappa_1^2 + 2\nu\kappa_1\kappa_2 + \kappa_2^2)}{48w(1 - \nu^2)}$$

Neglecting higher nonlinear terms in the surface energy, the surface energy of the top surface and the bottom surface are:

$$\Pi_{surface-top} = \frac{gh(w + 2w_0)^2 (f_1 \kappa_1 + f_2 \kappa_2)}{4w}$$

$$\Pi_{surface-bottom} = -\frac{f_e gh \kappa_1 w}{4}$$

The results can be further simplified by the following normalization:

$$U = \frac{48(1 - \nu^2)Eh}{f_1^2 gw} \Pi$$

$$F_i = 6(1 - \nu^2)f_i / f_1$$

$$K_i = \kappa_i EH^2 / f_1$$

Thus we have

$$U_g = \frac{(K_1 K_2)^2 (w + 2w_0)^6 f_1^2}{80w^2 E^2 h^6} = \frac{(K_1 K_2)^2 \lambda^6 f_1^2 w^4}{80E^2 h^6}$$

$$U_b = \lambda^2 (K_1^2 + 2\nu K_1 K_2 + K_2^2)$$

$$U_{surface-top} = 2\lambda^2 (F_1 K_1 + F_2 K_2)$$

$$\Pi_{surface-bottom} = -2F_e K_1$$

In the equations,

$$\lambda = \frac{(w+2w_0)}{w}, \tan(\theta) = \frac{w}{2g}, \beta = \frac{\lambda^6 f_1^2 w^4}{80E^2 h^6}$$

The total energy $U = U_g + U_b + U_{surface-top} + U_{surface-bottom}$

Let $\nabla U = 0$, taking derivatives with respect to K_i , we have

$$2\lambda^2 F_1 - 2F_e + 2\lambda^2(K_1 + K_2\nu) + 2\beta K_1 K_2^2 = 0$$

$$2\lambda^2 F_2 + 2\lambda^2(K_1\nu + K_2) + 2\beta K_2 K_1^2 = 0$$

The Hessian matrix is

$$H(\Pi) = \begin{bmatrix} 2\lambda^2 + 2\beta K_2^2 & 2\lambda^2\nu + 4\beta K_1 K_2 \\ 2\lambda^2\nu + 4\beta K_1 K_2 & 2\lambda^2 + 2\beta K_1^2 \end{bmatrix}$$

For a minimum energy configuration, the determinant of Hessian matrix needs to be positive so that the matrix is positive-definite.

In the analysis of the Figure 2 in the main text, we used $E= 170$ GPa, $\nu_{yy}= 0.36$, $h=35$ nm, $w=3690$ nm, $w_0= 20$ nm, $f_1=1$ and $\theta=\pi/12$. We obtained the result in Figure 2 by fixing the surface stress on the top and increasing the surface stress on the bottom f_e ,

Further analysis shows that when $F_1 = F_2$, $F_e = 0$ we can have an analytical result. Subtracting the two equations, we have

$$[2\lambda^2(1 - \nu) - 2\beta K_1 K_2](K_1 - K_2) = 0$$

when $K_1 = K_2$, the equation becomes

$$2\lambda^2 F_1 + 2\lambda^2 K_1(1 + \nu) + 2\beta K_1^3 = 0$$

The discriminant $\Delta = -8\beta[2\lambda^2(1 + \nu)]^3 - 432\beta^2\lambda^4 F_1^2 < 0$, so there is only one root.

When $K_1 K_2 = \frac{\lambda^2(1-\nu)}{\beta}$, the equation becomes

$$2\lambda^2 F_1 + 2\lambda^2(K_1 + K_2) = 0$$

We have $k_{1,2} = \frac{1}{2} \left(F_1 \pm \sqrt{F_1^2 - 4 \frac{\lambda^2(1-\nu)}{\beta}} \right)$

4. Finite Element Modeling

A three-dimensional computational model was built in ABAQUS V6.14. The mesh geometry for the full micro-claw has a total of 3825 nodes and 4664 elements using the quadratic element C3D20. In the micro-claw modeling, the Cr layer is assigned isotropic properties with a modulus of 377 GPa and a Poisson's ratio of 0.28. The orthotropic properties of the Si layer were set by nine engineering constants: $E_{xx}=E_{yy}=130$ GPa; $E_{zz}=170$ GPa; $\nu_{xx}=\nu_{yy}=0.36$; $\nu_{zz}=0.28$; $G_{xy}=G_{yz}=80$ GPa; $G_{xz}=50$ GPa. Since we only model a triangular "finger" from the micro-claw, the boundary conditions define with a fixed point on the mid-span of the Si layer and a symmetric condition to constrain the rotation of the edge plane. We used the static general solver with artificial damping which has proven to be a robust and reliable analysis for snap-through problems.^{3,4}

We define four simple *STATIC steps including large deformation (*NLGEOM). In the first step, the known 1.5% tensile strain of the Cr layer was converted to stress (5.65 GPa) by multiplying the in-plane property and added to the Cr layer as a predefined mechanical stress field. We used the partition tool in ABAQUS to cut the underetching width from the bottom layer and applied a temperature field to simulate the edge effect. The Si layer is subjected to an initial temperature of 130°C and a final temperature of 30°C to all of the nodes of the model. We define an anisotropic thermal expansion coefficient to the Si layer with a magnitude of $2 \times 10^{-6}/^{\circ}\text{C}$ perpendicular to the edge and zero for other two directions, which result as the edge effect. The manipulation in the third step is also performed with a cool-down temperature field to -70°C to simulate an external force to the layer. In the final step, we did a heat-up analysis by increasing the temperature back to 30°C such that the additional force can be removed. The advantage of such an approach is that no contact loads need to be applied on the structure, which avoids potential convergence issues. Artificial damping is added to the whole system to improve convergence by setting the dissipated energy fraction to 0.0002 in "Automatic Stabilization". Finally, the criterion on bistability depends on removing the temperature loads to see whether the new configuration is stable.

5. The Effect of Underetching Width on the Edge

We used the same theoretical framework to study the change of the bistable regime under different underetching widths. Figure S3 shows the transition of the bistable regime with $w_0=200$ nm and $w_0=500$ nm. This result is consistent with the numerical prediction, indicating that the onset of bistability as edge stress is increased is delayed by increasing the underetching width. The reason for such delay is due to the decrease of the total area of the bottom layer, which requires a greater contribution from the edge stress to overcome the stretching energy of the top layer and make the whole bilayer structure to snap through. It is also interesting to find that the size of the bistable regime decreases as the edge stress increase.

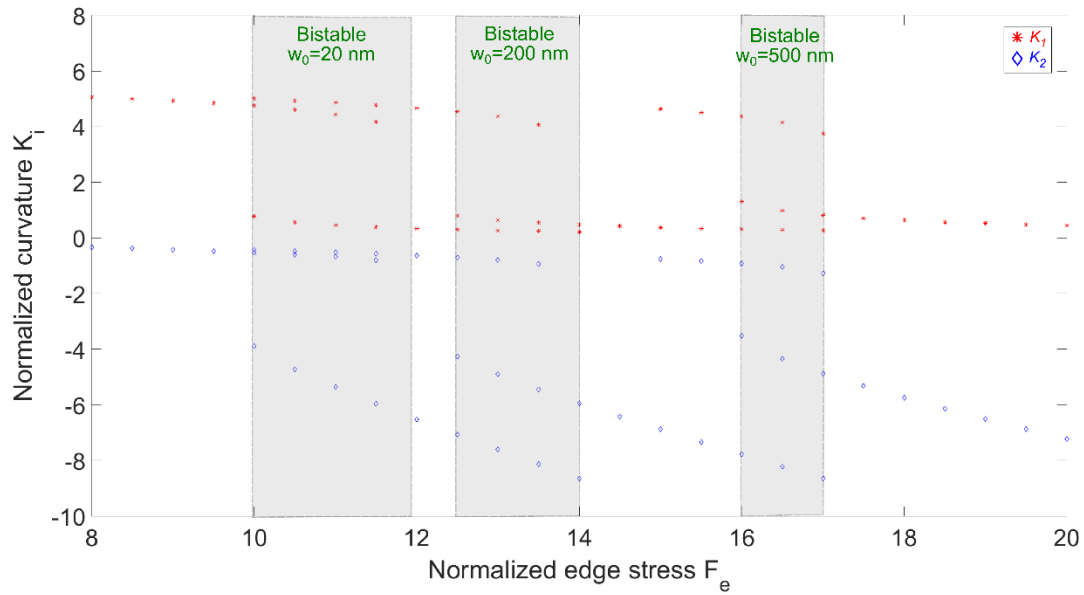


Figure S3. The offset of the bistable regime due to increasing underetching width.

REFERENCES

1. Zhang, L.; Dong, L.; Bell, D. J.; Nelson, B. J.; Gruetzmacher, D. A. In *Fabrication and Characterization of Self-scrolling Si/Cr Micro- and Nanostructures, Nano/Micro Engineered and Molecular Systems*, 2006. NEMS '06. 1st IEEE International Conference on, 18-21 Jan. 2006, 2006; pp 1268-1271.
2. Chen, Z.; Guo, Q.; Majidi, C.; Chen, W.; Srolovitz, D. J.; Haataja, M. P. *Physical Review Letters* 2012, 109, (11), 114302.
3. Portela, P.; Camanho, P.; Weaver, P.; Bond, I. *Computers & Structures* 2008, 86, (3-5), 347-356.
4. Mattioni, F.; Weaver, P. M.; Potter, K. D.; Friswell, M. I. *International Journal of Solids and Structures* 2008, 45, (2), 657-675.